Matter and Radiation at Extremes

RESEARCH ARTICLE | SEPTEMBER 20 2024

Ultrarelativistic Fe plasma with GJ/cm³ energy density created by femtosecond laser pulses

Mariya Alkhimova ; Igor Skobelev ; Tatiana Pikuz ; Sergey Ryazantsev ; Hironao Sakaki ; Alexander S. Pirozhkov ; Timur Zh. Esirkepov ; Akito Sagisaka; Nicholas P. Dover ; Kotaro Kondo; Koichi Ogura; Yuji Fukuda ; Hiromitsu Kiriyama; Keita Nishitani; Sergey Pikuz ; Masaki Kando ; Ryosuke Kodama; Kiminori Kondo ; Mamiko Nishiuchi

Check for updates

Matter Radiat. Extremes 9, 067205 (2024)
https://doi.org/10.1063/5.0212545

View Online Export Citation

Articles You May Be Interested In

Longitudinal electrostatic waves in isotropic thermal plasmas: Ultrarelativistic pair plasmas
Phys. Plasmas (August 2019)

Short-wavelength soliton in ultrarelativistic electron–positron–ion plasmas
Phys. Plasmas (July 2021)

Evolution of magnetohydrodynamic waves and associated ultrarelativistic electron acceleration
Phys. Plasmas (September 2011)

04 August 2025 07:51:07

AIP Publishing

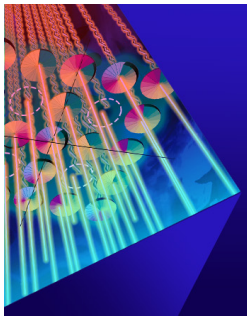

Matter and Radiation at Extremes
Special Topics Now Online
Read Now
AIP Publishing

Matter and Radiation at Extremes | RESEARCH ARTICLE | pubs.aip.org/aip/mre

Ultrarelativistic Fe plasma with GJ/cm^3 energy density created by femtosecond laser pulses

Cite as: Matter Radiat. Extremes 9, 067205 (2024); doi: 10.1063/5.0212545
Submitted: 5 April 2024 • Accepted: 22 August 2024 •
Published Online: 20 September 2024

View Online Export Citation CrossMark

Mariya Alkhimova,[1,a)] Igor Skobelev,[1] Tatiana Pikuz,[3] Sergey Ryazantsev,[1,4] Hironao Sakaki,[5] Alexander S. Pirozhkov,[5] Timur Zh. Esirkepov,[5] Akito Sagisaka,[5] Nicholas P. Dover,[5] Kotaro Kondo,[5] Koichi Ogura,[5] Yuji Fukuda,[5] Hiromitsu Kiriyama,[5] Keita Nishitani,[6] Sergey Pikuz,[4] Masaki Kando,[5] Ryosuke Kodama,[3,4] Kiminori Kondo,[5] and Mamiko Nishiuchi[5]

AFFILIATIONS

[1] Joint Institute for High Temperatures, Russian Academy of Sciences, Moscow 125412, Russia
[2] National Research Nuclear University (MEPhI), Moscow 115409, Russia
[3] Institute for Open and Transdisciplinary Research Initiatives, Osaka University, 2-6 Yamadaoka, Suita, Osaka 565-0871, Japan
[4] HB11 Energy Holdings Pty, 11 Wyndora Ave., Freshwater, New South Wales 2096, Australia
[5] Kansai Institute for Photon Science (KPSI), National Institutes for Quantum Science and Technology (QST), 8-1-7 Umemidai, Kizugawa, Kyoto 619-0215, Japan
[6] Interdisciplinary Graduate School of Engineering Sciences, Kyushu University, 6-1 Kasugakoen, Kasuga, Fukuoka 816-8580, Japan

[a)] **Author to whom correspondence should be addressed:** maryalkhimova@ihed.ras.ru

ABSTRACT

The generation of a plasma with an ultrahigh energy density of 1.2 GJ/cm^3 (which corresponds to about 12 Gbar pressure) is investigated by irradiating thin stainless-steel foils with high-contrast femtosecond laser pulses with relativistic intensities of up to 10^{22} W/cm^2. The plasma parameters are determined by X-ray spectroscopy. The results show that most of the laser energy is absorbed by the plasma at solid density, indicating that no pre-plasma is generated in the current experimental setup.

© 2024 Author(s). All article content, except where otherwise noted, is licensed under a Creative Commons Attribution (CC BY) license (https://creativecommons.org/licenses/by/4.0/). https://doi.org/10.1063/5.0212545

I. INTRODUCTION

The investigation of states of matter with high energy density (>10^5 J/cm^3) is of great interest across various scientific fields, including astrophysics,[1,2] strong-interaction physics,[3] plasma physics and thermonuclear fusion,[4,5] physics at high voltage and high power,[6–8] and particle acceleration techniques.[9,10] Creating such extreme states of matter in the laboratory typically involves compression of heated matter or plasma using shock waves induced by various tools such as gas guns, pinching discharges, and high-power lasers.[11–13] If it becomes possible to provide a high initial density of matter through the use of solid targets and rather short durations of the heating pulse ($\tau_{las} \ll \tau_{exp} \sim l_{plasma}/v_s$, where l_{plasma} is the plasma size and v_s is the ion-acoustic velocity), then high-energy-density conditions can be created at least for times not exceeding the plasma expansion time τ_{exp}. Note that for times shorter than τ_{exp}, the expansion of the plasma is one-dimensional and its density decreases slowly, but for $t > \tau_{exp}$, the plasma expansion becomes three-dimensional and its density decreases rapidly. When a laser pulse interacts with a target, the size of the directly heated area d_{plasma} is almost equal to the focal spot and is 1–10 μm. The expansion velocity of the ions is the ion-acoustic velocity, which is not strongly dependent on the plasma temperature and has a typical value of about 10^7 cm/s. The condition $\tau_{las} < \tau_{exp}$ requires laser pulses with a duration of femtoseconds (τ_{las} < 10–100 fs). To achieve this, femtosecond lasers with relativistic intensity can be used. There has been significant progress in the development of these lasers during the last ten years.[14–17]

The use of ultra-intense ultrashort pulses enables higher temperatures of the heated electrons and a higher electron density to be achieved.

However, it is possible to increase the density in the absorption region if an ultrashort pulse irradiates targets that have not undergone significant expansion on the front side. In this case, the

04 August 2025 07:51:07

© Author(s) 2024

laser energy couples directly into the solid-density material, and the electron density significantly exceeds the critical density. This enables the generation of a plasma with ultrahigh energy density (>10^8 J/cm^3). However, it requires very high-contrast laser pulses to exclude target expansion during the laser prepulse.[14]

In this work, we investigate the conditions that allow the generation of an ultrahigh density, ultra-high-temperature plasma with an energy density of more than 10^8 J/cm^3 and a pressure of more than 1 Gbar. We investigate plasma parameters measured by X-ray spectroscopic approaches when targets are driven with a femtosecond laser pulse with a laser intensity on the target of up to 5 × 10^{21} W/cm^2. When the laser contrast is insufficient, but an ultrahigh laser pulse is maintained, the energy concentration in the plasma is still high, owing to the high relativistic critical density, but significantly lower than in the case of solid-density plasma formation. In practice, measuring the laser contrast in the 10^{12}–10^{15} range is challenging, and it is difficult to determine the contrast level of single shots in advance. Nevertheless, by diagnosing the parameters of the generated plasma, we can deduce the state of the target at the time of the main laser pulse. If the target remains solid, this indicates that the laser contrast is sufficient to minimize the pre-plasma effects. In Ref. 18, it is shown that at a laser intensity of ~10^{20} W/cm^2, a typical laser contrast of 10^{10} is required to eliminate pre-plasma effects and that the requirements increase with increasing laser intensity.

II. EXPERIMENT

A. Experimental setup

The experiments were performed at the J-KAREN-P laser facility at the Kansai Photon Science Institute, Japan. The laser is a PW-class hybrid laser system that combines optical parametric chirped pulse amplification (OPCPA) and Ti:Sa chirped pulse amplification technology. In the current experiments, the J-KAREN-P laser operated at a wavelength of 800 nm and delivered high-contrast (up to 10^{12}) pulses with a duration t ~ 40 fs and an intensity I_{lt} of up to 5 × 10^{21} W/cm^2 on the target.[16,19,20]

In our experiments, we systematically investigated the plasma of thin stainless-steel foils under different laser conditions: on-target intensity < 10^{21} W/cm^2 and high contrast > 10^{10} (referred to as case A); on-target intensity > 10^{21} W/cm^2 and low contrast 10^5–10^6 (case B); and on-target intensity > 10^{21} W/cm^2 and high contrast ~10^{12} (case C). The laser contrast was measured using a Sequoia cross-correlator (Amplitude Technologies). The parameters of the generated plasma, namely, its electron temperature T_e and electron density N_e, were measured using high-resolution X-ray spectroscopy. A sketch of the experimental setup is shown in Fig. 1. The laser beam irradiated a stainless-steel foil (SUS, type AISI 304: Fe 72%, Cr 18%, Ni 10%) with thickness 2 or 5 μm at an angle of 45° to the normal to the target surface. The p-polarized beam was focused by an off-axis parabolic mirror with f/1.3 into a focal spot with diameter d ~ 2–4 μm.

The X-ray spectra of the plasma emission were detected by a focusing spectrometer with spatial resolution (FSSR)[21] with a spectral resolution $\lambda/\delta\lambda$ ~ 3000. The spectrometer was installed at a distance of 2045 mm from the plasma source to provide registration of spectra emitted from the front side of the SUS foil surface at an observation angle ~8° to the target surface normal.

The spectrometer was equipped with a spherically bent mica crystal with radius of curvature R = 150 mm and lattice spacing $2d$ = 19.94 Å or an alpha-quartz crystal with $2d$ = 2.36 Å (orientation 31–40, radius of curvature R = 150 mm). X-ray spectra were detected by an Andor DX-440 X-ray CCD with pixel size 13.5 μm. The CCD matrix was protected against exposure to visible light by two layers of 1 μm-thick polypropylene coated with 0.2 μm Al. In all experiments, the spectrometer was aligned to measure K-shell emission of multiply charged Fe XXV and Fe XXVI ions (lines He$_\alpha$, and Ly$_\alpha$) and the characteristic lines $K_{\alpha,\beta}$ of the Fe I ion in the wavelength range 1.74–1.97 Å. This observation range corresponds to the eighth (m = 8) diffraction order of the mica crystal and the first diffraction order of the α-quartz crystal. To suppress the contribution of plasma emission in the low diffraction orders of the mica, we placed a Mylar ($C_{10}H_8O_4$) film in front of the crystal. The thickness of the Mylar film was varied from 6 to 100 μm. As already mentioned, the

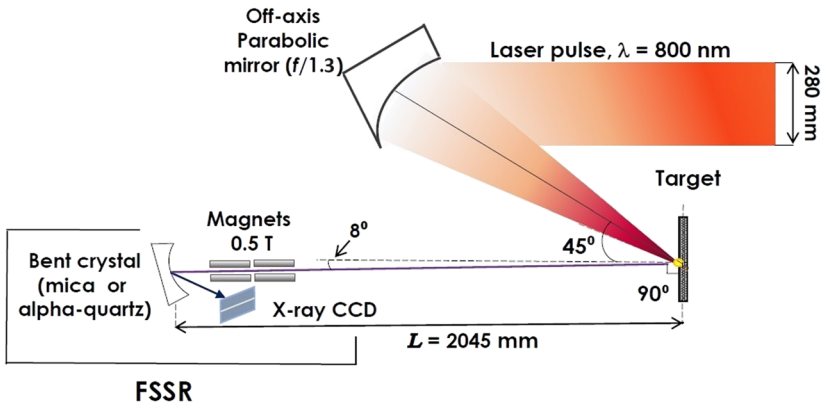

FIG. 1. Experimental setup. A femtosecond laser pulse with wavelength λ = 800 nm is focused at an angle of 45° onto the surface of a steel foil target in a focal spot with a diameter of 2–4 μm to generate a plasma on the front surface of the target. The X-rays from the plasma are measured by the X-ray focusing spectrometer (FSSR) positioned at a distance L = 2045 mm from the plasma source at an angle of 8° to the normal to the target surface.

04 August 2025 07:51:07

© Author(s) 2024

TABLE I. Main parameters of three experiments (cases A, B, and C) performed at the J-KAREN-P laser facility.

Parameter	J-KAREN, case A	J-KAREN-P, case B	J-KAREN-P, case C
Energy (J)	7	14	9
Pulse duration (fs)	35	35	40
Focal spot diameter (μm)	6.5	4	3
Laser intensity (W/cm^2)	6×10^{20}	3×10^{21}	5×10^{21}
Laser contrast	$>10^{10}$	10^5–10^6	$>10^{12}$
Target thickness (μm)	2	5	5
FSSR crystal	Alpha-quartz, $2d$ = 2.36 Å	Mica, $2d$ = 19.94 Å	Alpha-quartz, $2d$ = 2.36 Å
X-ray spectrum	Figure 2(a)	Figure 2(b)	Figure 2(c)

experiments were carried out for different laser operating regimes that differed primarily in terms of laser contrast and laser intensity on the target surface. The parameters of the experiments are listed in Table I. The measured X-ray spectra emitted by the SUS plasma in the spectral range 1.73–1.97 Å are shown in Fig. 2. The X-ray spectra shown in Figs. 2(a)–2(c) correspond respectively to the experimental conditions of cases A, B, and C described in Table I.

First, we compare the spectra measured in the experimental cases A and B. Figure 2(a) clearly shows that the intensity of the Fe He$_\alpha$ line is lower, although experiment B was performed with a higher laser pulse energy (14 vs 7 J in experiment A) and intensity (3×10^{21} W/cm^2 vs 6×10^{20} W/cm^2 in experimental case A. In the spectrum shown in Fig. 2(b), the He$_\alpha$ line of Fe XXV is very poorly separated from the noise, whereas it is well defined in the spectrum in Fig. 2(a).

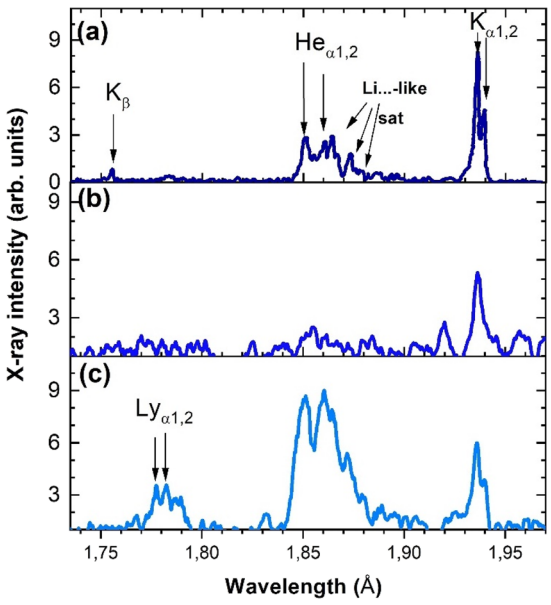

FIG. 2. X-ray spectra of stainless-steel plasma measured under the experimental conditions described in Table I: (a) case A; (b) case B; (c) case C.

In case B, the laser contrast is much poorer. This means that the drop in laser contrast to values of 10^5–10^6 leads to pre-plasma formation, which drastically (up to two orders of magnitude) decreases the density of the heated plasma and consequently increases the time required to complete the ionization processes by up to two orders. The observed absence of He- and H-like iron lines in the spectrum in Fig. 2(b) makes it impossible to apply X-ray spectroscopic approaches based on the consideration of line emission spectra. Nevertheless, information about the temperature of the bulk of the plasma electrons can be obtained by analyzing the continuous spectrum due to bremsstrahlung, as was done in Refs. 22 and 23. The detailed calculation of the X-ray spectrum measured in case A is presented in Ref. 24 and will not be discussed in detail here. The X-ray spectrum measured in case C is shown in Fig. 2(c). This spectrum is particularly interesting because, as we will see below, it corresponds to the case in which no pre-plasma is formed, and it becomes possible to heat the solid target to high keV temperatures and generate a plasma with an energy density of ~1 GJ/cm^3. In contrast to the spectra in Figs. 2(a) and 2(b), the spectrum in Fig. 2(c) contains intense lines corresponding to the transitions in H- and He-like Fe ions. These can be used to determine the plasma parameters using the following X-ray spectroscopic approaches.

B. Diagnostics approaches

Note that in experiments with ultrahigh laser intensities, the deviation of the contrast level from shot to shot, as well as the deviation of other pulse parameters, can be significant. Therefore, the question arises as to whether it is possible to determine the creation of the pre-plasma with other diagnostic methods.

We propose the use of two X-ray spectroscopic approaches for this purpose. The first approach allows a clear distinction of the conditions for the interaction of the laser pulse with the target when the main pulse is shielded by a pre-plasma or when no pre-plasma occurs, and an ultrahigh energy density plasma is generated. The second approach is based on registering and analyzing specific features that can only appear in the emission spectrum if the plasma has a high density.[25,26] These are first, a broadening of the spectral lines due to the Stark effect and, second, the relative intensities of certain transitions in multiply charged ions (see, e.g., Ref. 27).

In our case, the spectral feature in the range of Fe XXV and Fe XXVI ions (lines He$_{\alpha1}$ = 1.85 Å, He$_{\alpha2}$ = 1.86 Å, and Ly$_{\alpha1}$ = 1.77 Å, Ly$_{\alpha2}$ = 1.78 Å) and characteristic lines K_α = 1.94 Å (K_β = 1.76 Å)

04 August 2025 07:51:07

© Author(s) 2024

of Fe are under consideration. Note that since the measurements of X-ray emission from the femtosecond laser plasma were performed without time resolution, each observed spectrum represents a time-integrated plasma glow consisting of emissions corresponding to the decay of the dense plasma state. As a result, typical spectral features of a dense plasma could be overlapped by spectral features emitted at a later time of the plasma's existence. Two diagnostic approaches can therefore be used to investigate the interaction between the laser pulse and the dense plasma.

The idea of this first approach is that the time of collisional ionization in the plasma is inversely proportional to the plasma density. Thus, if one knows to some approximation the lifetime of the plasma in the hot state and uses a time-dependent kinetics calculation, one can find maximum ionization states for each ion that correspond to the solid or critical electron plasma density.

If the experimental spectrum shows lines emitted by ions in states that can only be observed in a solid-density plasma, this clearly indicates the absence of a pre-plasma in this experiment. As the ionization time for solid and critical density would differ by two to three orders of magnitude, the inaccuracy in the plasma lifetime estimation may be considered negligible. This approach has already been used in Ref. 24 to investigate the influence of laser pulse contrast on femtosecond laser plasma formation in stainless-steel foils. The method described is suitable for diagnosing pre-plasma formation, although it cannot be used to obtain detailed information about the plasma parameters.

The second diagnostic approach is based on the comparison of experimentally measured spectra with corresponding modeled spectra. It provides more detailed information about the plasma parameters but is more complex and difficult to apply for the following reasons.

In our case, the plasma parameters change rapidly both along and perpendicular to the target surface. To achieve a high laser intensity, the laser beam is usually focused on a focal spot with a diameter of ~1.5 to 10 μm. Accordingly, the plasma parameters change considerably in the same spatial dimensions. At such dimensions, the spectra of the plasma emission cannot be detected with spatial resolution. The measured spectra are therefore a superposition of X-ray spectra emitted by plasma regions (zones) with very different properties. Since the plasma parameters are continuous functions of the spatial coordinates, it is necessary for an adequate description of the observed spectra to consider a number of plasma zones with different parameters, as has been shown in Refs. 24 and 28–30. It is usually sufficient to consider two to three zones. The concept of plasma zones is illustrated in Fig. 3.

The first plasma zone, zone 1 obviously corresponds to the plasma region in which most of the energy of the laser pulse is absorbed. Zone 1 has a transverse size that corresponds to the size of the laser focal spot. If the wavelength of the heating laser pulse is ~0.8 μm and its intensity is a relativistic intensity $I_{las} \sim 10^{18}$ to 10^{21} W/cm^2, the existence of a high-intensity laser prepulse leads to the formation of a pre-plasma in the focal spot region. This plasma can reach an electron density around the critical electron density.[24,30] However, at ultra-relativistic laser intensities $I_{las} > 10^{21}$ W/cm^2, the plasma density in zone 1 becomes much higher, and, under certain experimental conditions,[22,31] increases to the value of the relativistic critical density or remains a solid density. Zone 2 is next to zone 1 and is heated by energy transfer processes from zone 1.

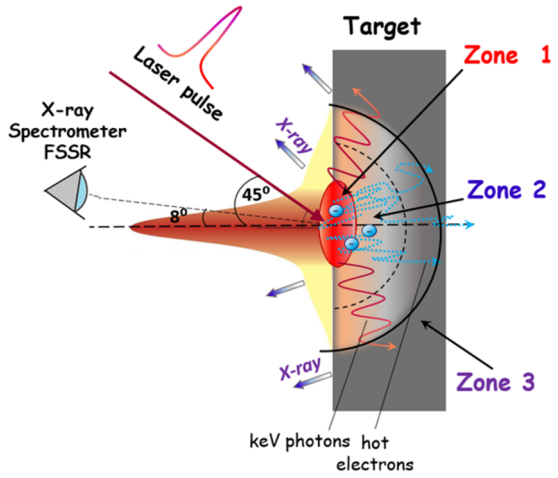

FIG. 3. Sketch of femtosecond ultra-intense laser pulse interaction with foil in the plasma zone concept.

Plasma zone 3 is the area of the solid target at a considerable distance from the laser beam axis. The heating of zone 3 is mainly due to hot electrons or intense X-ray photons emitted from the first zone. We therefore assume that the ion density in zones 2 and 3 is equal to the solid density $N_{i2} = N_{i3} = N_{i,\mathrm{solid}}$. However, the density in zone 1 could be a solid density $N_{i1} = N_{i,\mathrm{solid}}$ if there were no laser prepulse, or, depending on the laser intensity and prepulse, a density corresponding to the relativistic critical density $N_{e1} = N_{\mathrm{cr,rel}}$ or the nonrelativistic critical density $N_{e1} = N_{e,\mathrm{cr}}$. This approach suggests that the electron temperature decreases from zone 1 to zone 3, i.e., $T_{e1} > T_{e2} > T_{e3}$.

If the observed spectrum can be described by a sum of emission spectra from zones with different plasma parameters and if the hottest zone has the electron density N_{e1}, then, by comparing N_{e1} with the solid density and the relativistic critical density, it is possible to derive a plasma density in the region where the main laser pulse has mostly been absorbed. It is also possible to directly estimate the energy density of the free plasma particles. The validity of the second approach requires the presence of a sufficient number of spectral transitions in the measured spectra. In addition, a high spectral resolution of the X-ray spectra must be provided. The implementation of the second approach for the spectrum measured in case C is discussed in Sec. III B.

III. RESULTS AND DISCUSSION

A. Calculation of time dependence of formation of He-like and H-like Fe ions

First, we use the first diagnostic approach and consider the time dependences of the formation of He-like Fe XXV and H-like Fe XXVI ions in plasmas with different electron densities and electron temperatures (Fig. 4). Calculations are performed under the assumption of a time-dependent radiational–collisional kinetic model using the computational code PrismSPECT[32–34] for the following cases: a solid-density plasma with temperature 3000 eV (shown in black in Fig. 4), relativistic-density plasmas at laser intensities

04 August 2025 07:51:07

© Author(s) 2024

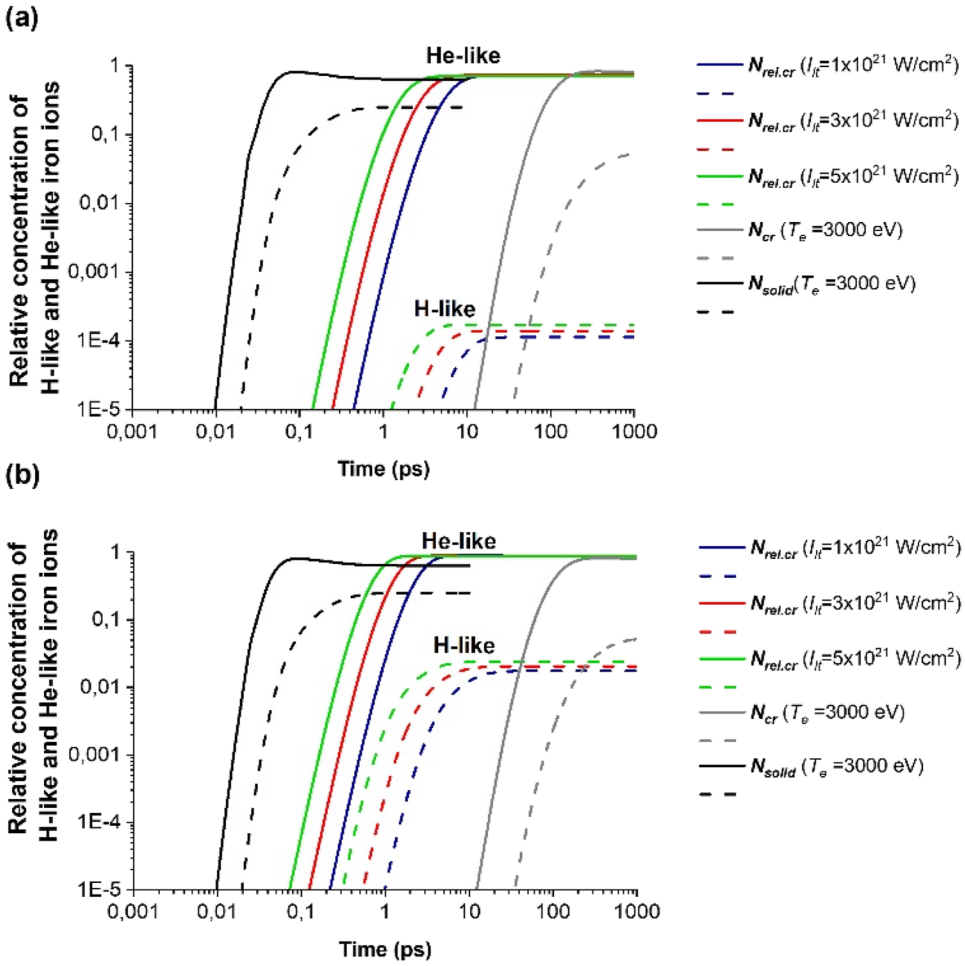

FIG. 4. Time dependences of concentrations of He-like Fe XXV (solid lines) and H-like Fe XXVI (dashed lines) ions calculated for electron temperatures of 1000 eV (a) and 2000 eV (b) and critical plasma densities, correspondent to different laser intensities (in different colors). Black curves correspond to the case of solid density ($N_{i,\mathrm{solid}}$ = 8 × 10^{22} cm^{-3}) and electron temperature T_e = 3000 eV. Gray curves correspond to the case of nonrelativistic critical density ($N_{e,\mathrm{cr}}$ ~ 1 × 10^{21} cm^{-3}) and electron temperature T_e = 3000 eV.

1 × 10^{21} W/cm^2 (in blue), 3 × 10^{21} W/cm^2 (in red), and 5 × 10^{21} W/cm^2 (in green) with temperatures 1000 eV [Fig. 4(a)] and 2000 eV [Fig. 4(b)] and a critical-density plasma with temperature 3000 eV (in gray). In all cases, the dependences for He-like and H-like Fe ions are indicated by solid and dashed lines, respectively. The calculation results showing the typical plasma lifetime for the formation of He-like Fe XXV and H-like Fe XXVI ions are presented in Table II.

As we can see from Table II and Fig. 4, the Fe ions with main K shell can only be produced at a reasonable plasma lifetime if the plasma density notably exceeds its nonrelativistic critical value $N_{e,\mathrm{cr}}$ ~ 10^{21} cm^{-3}. Generation of H-like Fe ions is only possible at laser intensities $I_{\mathrm{lt}} \geq 10^{21}$ W/cm^2, i.e., if the plasma electron density is not less than 3 × 10^{22} cm^{-3} and corresponds to the relativistic critical density. The formation of H-like Fe states becomes more effective in the case of a plasma with a solid density that is heated to a temperature of ~3000 eV (see Table II).

As can be seen in Fig. 2(a), the laser contrast increases up to 10^{10}, and so the spectral lines of He-like Fe XXV ions can be observed continuously even at a laser intensity I_{lt} ~ 6 × 10^{20} W/cm^2, which is lower than in case B. At the same time, the emission of H-like states is almost absent in the spectrum. From the calculations shown in Fig. 4(b), it follows that the plasma density in the focal spot region must have a relativistic critical density to enable such conditions to be achieved within a plasma lifetime of the order of a few picoseconds. This was also shown in Ref. 35.

Let us now look at the spectrum in Fig. 2(c), in which many intense Fe lines of the K shell can be seen. First, we note that the presence of bright emission of H-like Fe XXVI ions in the spectral region of the Ly$_\alpha$ line, together with the calculations shown in Fig. 4(b), suggests that the plasma formed under experimental conditions in case C has a bulk electron temperature of the order of 2000 eV and a density higher than the critical density. The observation of intense

04 August 2025 07:51:07

© Author(s) 2024

TABLE II. Results of the calculation of the time dependence of the formation of He-like Fe XXV and H-like Fe XXVI ions in plasmas with different electron densities and electron temperatures.

Plasma density type	Plasma density (cm^{-3})	Plasma temperature T_e (eV)	Time for He-like Fe XXV ion formation (ps)	Time for H-like Fe XXVI ion formation (ps)
Nonrelativistic critical electron density	$N_{e,cr} \sim 1 \times 10^{21}$	3000	10–20	70–100
Solid ion density	$N_{i,solid} = 8 \times 10^{22}$		0.01–0.02	0.05–0.08
Relativistic critical electron density for $I_{lt} \sim 1 \times 10^{21}$ W/cm^2	$N_{rel,cr} \sim 3 \times 10^{22}$	2000	0.2–0.3	1–2
Relativistic critical electron density for $I_{lt} \sim 3 \times 10^{21}$ W/cm^2	$N_{rel,cr} \sim 5 \times 10^{22}$		0.1–0.2	0.6–1
Relativistic critical electron density for $I_{lt} \sim 5 \times 10^{21}$ W/cm^2	$N_{rel,cr} \sim 6.5 \times 10^{22}$		0.07–0.1	0.1–0.3
Relativistic critical electron density for $I_{lt} \sim 1 \times 10^{21}$ W/cm^2	$N_{rel,cr} \sim 3 \times 10^{22}$	1000	1–2	10–20
Relativistic critical electron density for $I_{lt} \sim 3 \times 10^{21}$ W/cm^2	$N_{rel,cr} \sim 5 \times 10^{22}$		0.8–0.1	7–10
Relativistic critical electron density for $I_{lt} \sim 5 \times 10^{21}$ W/cm^2	$N_{rel,cr} \sim 6.5 \times 10^{22}$		0.2–0.3	2–4

well-resolved spectra of H- and He-like Fe ions allows us to apply our second approach to determine the plasma parameters.

B. Modeling of X-ray spectrum measured in experimental case C

To model the X-ray spectrum shown in Fig. 2(c), kinetic calculations are performed within the collisional–radiation model, including radiative transfer effects, using the computational code PrismSpect mentioned above. The plasma volume is divided into three plasma zones with significantly different parameters. Each zone is associated with the emission of specific spectral lines.

Let us consider X-ray emission from plasma zone 1. Since we have defined zone 1 as the hottest plasma region, the influence of K-shell emission from this zone is most important and should largely describe the emission of He- and H-like Fe ions. Good agreement between the modeling and the experimental spectrum can best be achieved by varying the values of T_{e1}, N_{e1}, and the plasma thickness l_1. In our considerations, the transverse size of the first plasma zone $d_{plasma1}$ cannot be larger than the diameter of the laser focal spot. The parameter $d_{plasma1}$ is limited by $d_{plasma} \leq 2$ μm. The longitudinal thickness of the plasma l_1 is defined by the expansion of the plasma perpendicular to the surface of the target. Assuming a one-dimensional expansion, the plasma thickness in zone 1 is estimated as $l_1 \sim 0.5$ μm in the case of $N_{e1} = N_{solid}$ or $l_1 \sim 2$ μm in the case of $N_{e1} = N_{rel,cr}$ (for a laser intensity of 5×10^{21} W/cm^2). The optical thickness of the plasma is considered using the Biberman–Holstein approximation for the escape factor.

We must emphasize that at an electron density corresponding to the nonrelativistic critical density $N_{e1} \sim 10^{21}$ cm^{-3}, the spectrum in Fig. 2(c) cannot be described by any values of plasma temperature or plasma size, including the case of an optically thin plasma ($l \to 0$). Figure 5 clearly shows this situation. The modeling in the large T_{e1} range from 1000 to 5000 eV (the red lines in Fig. 5) does not match

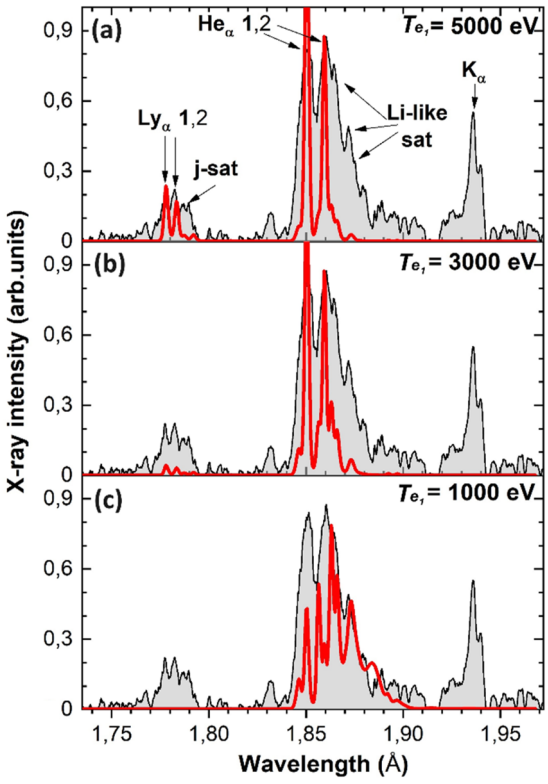

FIG. 5. Dependence of X-ray spectra emitted from plasma zone 1 with critical electron density ($N_{e1} = N_{e,cr} = 1 \times 10^{21}$ cm^{-3}) on the bulk electron temperature of the plasma T_{e1}; (a) $T_{e1} = 5000$ eV; (b) $T_{e1} = 3000$ eV; (c) $T_{e1} = 1000$ eV. The modeling results are shown by red lines. The X-ray spectrum measured in experimental case C is shown filled in with gray shading.

04 August 2025 07:51:07

© Author(s) 2024

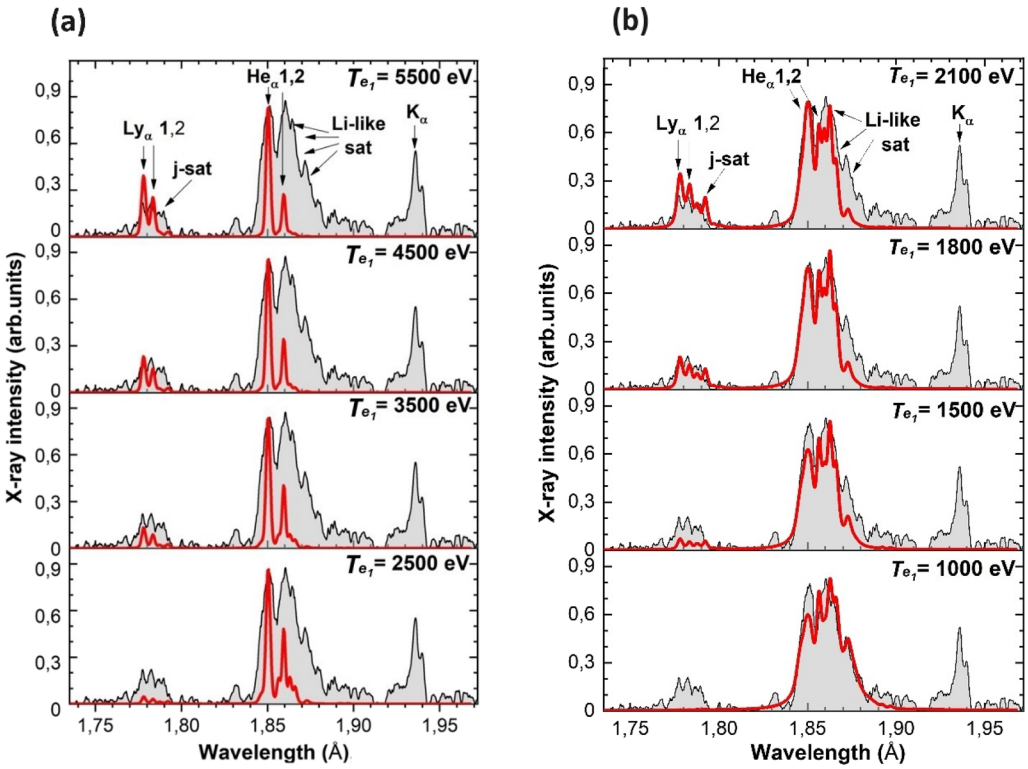

FIG. 6. Dependence of X-ray spectra emitted from plasma zone 1 on bulk plasma electron temperature: (a) for electron density $N_e = N_{rel,cr} = 6.5 \times 10^{22}$ cm^{-3} (the laser intensity of 5×10^{21} W/cm^2) and plasma thickness $l_1 \sim 2$ μm; (b) for solid density $N_{i,solid} = 8 \times 10^{22}$ cm^{-3} and plasma thickness $l_1 = 0.5$ μm. The modeling results are shown by red lines. The X-ray spectrum from Fig. 2(c) is shown filled in with gray shading.

the X-ray spectrum measured in experimental case C. Here and in all other figures, the X-ray spectrum measured in case C [see Fig. 2(c)] is shown filled in with gray shading for better illustration and easier differentiation from the modeling results.

At first glance, the choice of the relativistic critical density [see Fig. 6(a)] allows the ratio of the relative intensities of the Ly$_\alpha$ and He$_\alpha$ resonance lines to be described. However, as in the case of nonrelativistic critical density, the model calculations for the relativistic critical density cannot describe the experimental spectrum in the wavelength range 1.87–1.90 Å, in which the Li-like satellites of the He$_\alpha$ line are located. The situation changes significantly if it is assumed that the plasma generated in zone 1 has a solid density $N_{i,solid} = 8 \times 10^{22}$ cm^{-3}. For this case, the modeling results for different electron temperatures are shown in Fig. 6(b).

As can be seen in Fig. 6(b), we can describe the experimental spectrum near the Ly$_\alpha$ line and the experimental values of the relative intensities of the resonance lines (Ly$_{\alpha 1}$ and He$_{\alpha 1}$). Good agreement between modeling and measurements in the wide spectral range λ = 1.75–1.87 Å is achieved at a bulk plasma electron temperature T_{e1} = 1800 eV and a plasma thickness $l_1 = 0.5$ μm.

Since there are no lines associated with transitions in less-ionized Fe ions (Be-, B-, C- and N-like states) for this T_{e1} in the modeling spectrum, but these lines are present in the measured spectrum, we have considered the emission of these lines as radiation from plasma zone 2, which has a lower temperature. The modeling shows that the contribution of the satellite emission to the resulting intensity in the right wing of the He$_{\alpha 2}$ line depends strongly on the temperature and density (Figs. 7 and 8). Figure 7 shows the emission spectra of Fe ions calculated at a solid plasma ion density

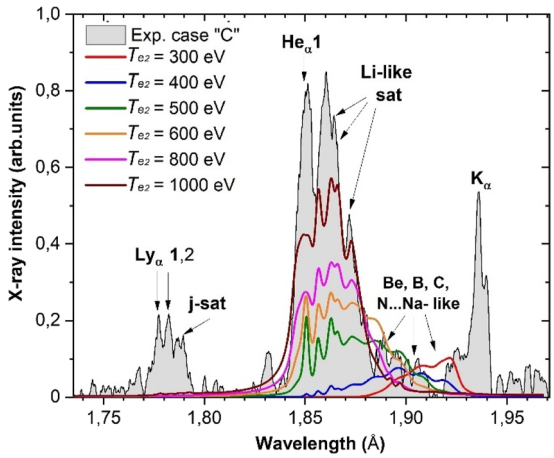

FIG. 7. Emission spectra of Fe plasma calculated at solid plasma ion density $N_{i,solid} = 8 \times 10^{22}$ cm^{-3} for different plasma temperatures T_e. The 0.1% of hot electrons with temperature T_{hot} = 10 keV are included in the calculations. The X-ray spectrum from Fig. 2(c) is shown filled in with gray shading.

04 August 2025 07:51:07

© Author(s) 2024

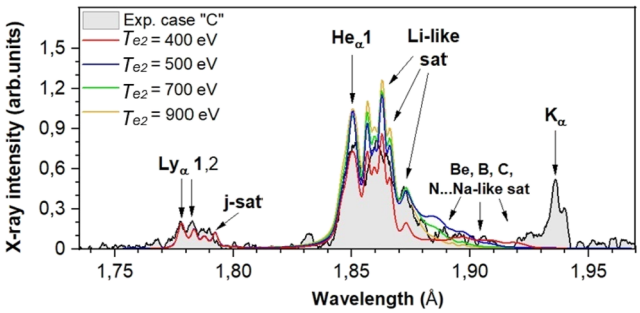

FIG. 8. Emission spectra of Fe plasma calculated as superpositions of emission spectra from zone 1 (T_{e1} = 1800 eV) with $N_{e1} = N_{solid}$ and from zone 2 at fixed plasma solid ion density $N_{i,solid} = 8 \times 10^{22}$ cm^{-3}, for different plasma temperatures, with the inclusion of 0.1% of hot electrons with temperature T_{hot} = 10 keV. The X-ray spectrum from Fig. 2(c) is shown filled in with gray shading.

$N_i = 8 \times 10^{22}$ cm^{-3} for different plasma temperatures. The 0.1% of hot electrons with a temperature T_{hot} = 10 keV were included in the calculations. We will show that the plasma temperature that allows a description of the Li-like Fe ion states is about $T_{e2} \sim 1000$ eV and that a temperature $T_{e2} \sim 500$ eV is required to describe the Be- and B-like states.

Let us now fix the ion density $N_{i,solid} = 8 \times 10^{22}$ cm^{-3} and consider together the modeling obtained for zone 1 at electron temperature T_{e1} = 1800 eV [Fig. 6(b), second from top] and the above result for zone 2. Figure 8 shows the sequence of spectra obtained as the sum of the spectra of zones 1 and 2 for different T_{e2} in the range 500–900 eV. The spectra are considered with equal weight coefficients. Figure 8 shows that the situation is still complicated. By adding a second plasma zone with $T_{e2} \sim 500$–900 eV, either the measured spectrum in the wavelength range 1.89–1.91 Å can be fitted, but with the description of the Li-like lines in the range 1.87–1.89 Å remaining incomplete, or conversely we can obtain good agreement between experiment and modeling for intense Li-like satellites, but with a large discrepancy in the range 1.88–1.91 Å.

Note that in both cases the relative intensity of the spectral lines in the range of 1.85–1.87 Å is significantly higher than the experimental values. The reason for this unsuccessful description of the spectrum is that the value chosen above T_{e1} = 1800 eV for zone 1, which correctly describes Ly_α with the satellites and correctly reflects the ratio of the relative intensities of the resonant $Ly_{\alpha1}$ and $He_{\alpha1}$ lines, was set too low.

This refers to the earlier assumption that the emission of He-like ions is only from the first plasma zone. However, in a solid-density plasma, spectral features associated with transitions in helium-like Fe ions appear to a small extent already at a temperature T_{e2} = 400 eV [see Fig. 6(b)]. For this reason, the resonance line $He_{\alpha1}$ cannot be considered as a spectral feature emitted only by zone 1. Therefore, it is necessary to find a T_{e1} at which the ratio $Ly_{\alpha1}/He_{\alpha1}$ corrects the modeled spectrum near $He_{\alpha1}$ and ensures good agreement in the spectral region including Ly_α and its satellites. The contribution to the sum of the modeled spectrum from each plasma zone must remain proportional.

It is obvious that choosing a higher T_{e1} requires a higher value for T_{e2}. For $T_{e1} \sim 2000$ eV, the relative intensities of the intercombination line $He_{\alpha2}$ and the Li-like satellites are already lower than the intensity of the resonance line $He_{\alpha1}$ [see Fig. 6(b)] and do not correspond to the experimental values. This inevitably leads to the choice of a T_{e2} that corresponds to an intense excitation of Li-like states and provides a sufficient contribution for zone 2 in the sum modeling the spectrum in the range 1.87–1.90 Å. Since lines of hydrogen-like Fe ions appear in the spectrum at $T_{e2} \geq 1100$ eV, this implies that the effects of zone 2 in the spectral region include Ly_α and its satellites. We also note that the choice of electron temperature in zone 1 has an upper limit of ~3000 eV, since at $T_{e1} > 2500$ eV, the contribution of zone 1 to the total spectrum is considerably lower than the contribution of zone 2.

In a few iterations, we gradually increase the plasma temperature in zone 1 from the lowest value T_{e1} = 1800 eV to T_{e1} = 3000 eV and adjust the corresponding electron temperature in the range 400 eV ≤ T_{e2} ≤ 1100 eV. We find that the best agreement between the modeled and measured spectra is achieved in a wide spectral range when considering the electron temperatures T_{e2} = 2500 eV and T_{e2} = 900 eV (see Fig. 9).

X-ray emission from the third, coldest, plasma zone 3 is connected with the appearance of the K_α line in the spectrum. This line corresponds to transitions in atoms and ions of iron with an ionization state not higher than 3. These states are generally caused by hot electrons that have heated the target to a temperature of a few tens of eV. The shape of the K_α line and its position in the spectrum can be used to determine the temperature of the plasma electrons in zone 3.[35] In case C, this temperature is $T_{e3} \sim 80$ (±30) eV.

If we sum the emission spectra from all three plasma zones, we obtain a good description of the experimentally observed spectrum in the entire observed spectral range. This can be seen in Fig. 10, which shows the X-ray spectrum measured in case C and the model spectrum calculated for the parameters listed in Table III.

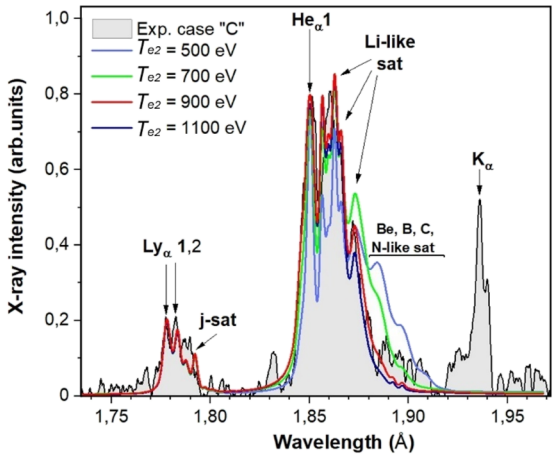

FIG. 9. Emission spectra of iron plasma calculated as superposition of emission spectra from zones 1 and 2 at fixed plasma solid ion density $N_{i,solid} = 8 \times 10^{22}$ cm^{-3} and a temperature in zone 1 of T_{e1} = 2500 eV for different plasma temperatures T_{e2}. The X-ray spectrum from Fig. 2(c) is shown filled in with gray shading.

04 August 2025 07:51:07

© Author(s) 2024

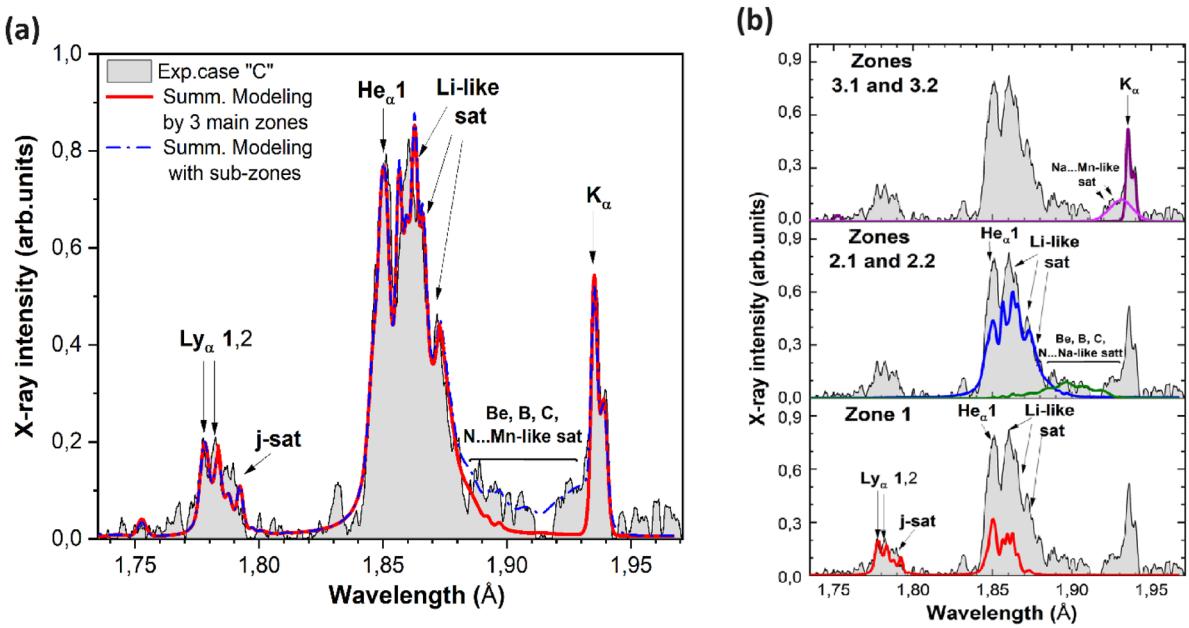

FIG. 10. Comparison of the results of kinetic modeling obtained under the assumption of X-ray emission from three different plasma zones and the experimentally measured spectrum for a laser intensity on target $I_{lt} = 5 \times 10^{21}$ W/cm^2. (a) Sum of the modeled spectra for the three main plasma zones compared with experimental case C. (b) Contributions of each plasma zone in the sum of the modeled spectra.

TABLE III. Plasma parameters used in the calculations to describe the X-ray spectrum measured in experimental case C.

Parameter	Zone 1	Zone 2	Zone 3
N_i (cm^{-3})	8×10^{22}	8×10^{22}	8×10^{22}
N_e (cm^{-3})	1.94×10^{24}	1.8×10^{24}	5.5×10^{23}
T_e (eV)	2500 (±200)	900 (±100)	80 (±30)
T_{hot} (keV)	0.1%, 10 keV	0.1%, 10 keV	0.1%, 10 keV
Electron energy density (J/cm^3)	1.2×10^9	0.4×10^9	1×10^7

As can be seen from Fig. 10, to describe the X-ray emission of the plasma generated by irradiating thin SUS foils with femtosecond laser pulses with ultrarelativistic intensities ($I_{lt} \sim 5 \times 10^{21}$ W/cm^2), it is necessary to consider at least three plasma regions. Of course, the consideration of three zones is a rather rough approximation that only describes the most intense parts of the observed spectrum well, but this is already sufficient for many cases.

If a more precise description of low-intensity spectral features in the 1.88–1.91 Å range is required, we can divide zone 2 into two subzones 2.1 and 2.2 with different electron temperatures and solid densities, as has been done in Ref. 22. For the spectrum in Fig. 2(c), which includes subzone 2.2 with $T_{e2.2} \sim 400$ eV, a more accurate agreement between modeling and experiment can be achieved in the wavelength range 1.88–1.91 Å (see the green curve in Fig. 10). Division of zone 3 into two subzones 3.1 and 3.2 with $T_{e3.1} \sim 170$ eV and $T_{e3.2} \sim 80$ eV also improves the agreement between modeling and experiment in the spectral region near the K_α line.

C. Discussion

In experimental high-energy-density physics, it is important not only to create the plasma in question, but also to measure (or at least estimate) its parameters. In the case of relativistic laser plasmas, the dimensions of the object are very small, owing to the necessity of using high laser intensities and consequently extremely small sizes of the focal laser spot. As a result, the dimensions of the object are smaller than or of the order of the spatial resolution of the X-ray spectrometer, and only spatially integrated emission spectra are available for diagnosis. At the same time, the relativistic plasma is very inhomogeneous despite its small size, and it is usually impossible to describe its emission spectrum, which is caused by transitions in ions of different multiplicity, by single values of density and temperature. A possible solution to this problem is to divide the entire plasma into several zones with different temperatures and densities. To prevent the number of free parameters from becoming too large, it is advisable to include as few zones as possible in the

04 August 2025 07:51:07

© Author(s) 2024

consideration, and the subdivision into zones should be physically justified by the predominance of certain physical processes in each of them.

In this paper, using the spectra of a Fe plasma as an example, we have shown that it is possible to estimate the probable value of the plasma density and electron temperature corresponding to the maximum ionization states for each ion (see Fig. 4 and Table II). We have demonstrated that it is sufficient to consider three plasma zones to describe the emission spectrum of H-, He-, and Li-like Fe ions. The good agreement between experimental measurements and the modeled X-ray spectrum gives confidence in the assumption of different plasma zones, allowing us to determine the electron temperature in each region. In particular, we have observed that the target region heated by the main laser pulse, zone 1, reaches $T_{e1} \sim 2500$ eV, while the peripheral target region around the focal point is heated to $T_{e2} \sim 900$ eV and the region far from the laser axis has a bulk electron temperature $T_{e3} \sim 80$ eV. An intriguing and unexpected observation is the absence of a plasma zone at the critical electron density $N_{e,\mathrm{cr}}$. This indicates that the laser contrast was high enough to prevent the formation of a pre-plasma and allow direct absorption of the laser energy in the solid-density target. This enabled the generation of record high energy densities of 1.2 GJ/cm^3 in the focal spot region and ~10 MJ/cm^3 in the peripheral target region.

IV. CONCLUSION

We have demonstrated the generation of matter with an energy density of ~1.2 GJ/cm^3 (which corresponds to about 12 Gbar pressure) in a laboratory experiment by the interaction of ultrarelativistic high-contrast femtosecond laser pulses with flat SUS foils. A further possibility to increase the energy density will be available with the commissioning of new laser systems with intensities of more than 10^{23} W/cm^2.[12,15,36] High-resolution X-ray spectroscopic methods are still effective to study the extreme states of matter produced in new-generation laser systems. However, a deeper understanding of the underlying physical processes requires more complex approaches to the modeling of spectra of multiply charged ions, including nonstationary cases.

ACKNOWLEDGMENTS

X-ray measurements, X-ray spectral simulations, and analysis were supported by the Ministry of Science and Higher Education of the Russian Federation (State Assignment No. 075-00270-24-00). Calculations were carried out on the computational resources of the JSCC RAS. The work was carried out within the framework of Program 10 "Experimental laboratory astrophysics and geophysics, NCPM."

AUTHOR DECLARATIONS

Conflict of Interest

The authors have no conflicts to disclose.

Author Contributions

M.N. led the project, M.A. and P.T. implemented diagnostics and provided the experimental data; M.N., H.S., A.S.P., A.S., N.P.D., Ko.K., K.O., Y.F., K.N., and M.K. performed the experiment; M.A., I.S., T.P., S.R., S.P., M.N., A.S.P., and T.E. analyzed data; M.A. and I.S. performed modeling and wrote the article; H.K., R.K., and K.K. supervised the project; all authors contributed to the discussion of results and review of the article.

Mariya Alkhimova: Data curation (equal); Formal analysis (equal); Investigation (equal); Resources (equal); Visualization (equal); Writing – original draft (equal); Writing – review & editing (equal). **Igor Skobelev**: Data curation (supporting); Formal analysis (equal); Software (equal); Supervision (supporting); Visualization (equal); Writing – original draft (supporting); Writing – review & editing (supporting). **Tatiana Pikuz**: Conceptualization (equal); Formal analysis (supporting); Investigation (equal); Supervision (supporting); Validation (equal); Writing – original draft (supporting); Writing – review & editing (supporting). **Sergey Ryazantsev**: Conceptualization (supporting); Data curation (supporting); Formal analysis (supporting). **Hironao Sakaki**: Data curation (supporting); Formal analysis (supporting); Investigation (equal); Writing – review & editing (supporting). **Alexander S. Pirozhkov**: Conceptualization (supporting); Investigation (equal); Methodology (equal); Resources (equal). **Timur Zh. Esirkepov**: Formal analysis (supporting); Methodology (supporting); Software (supporting). **Akito Sagisaka**: Data curation (supporting); Investigation (equal). **Nicholas P. Dover**: Data curation (supporting); Investigation (equal); Visualization (equal); Writing – review & editing (equal). **Kotaro Kondo**: Investigation (equal); Methodology (equal). **Koichi Ogura**: Formal analysis (supporting); Investigation (equal); Methodology (equal); Writing – review & editing (supporting). **Yuji Fukuda**: Conceptualization (equal); Data curation (equal); Formal analysis (equal); Investigation (equal); Resources (equal); Supervision (supporting). **Hiromitsu Kiriyama**: Conceptualization (equal); Formal analysis (equal); Investigation (equal); Software (lead); Supervision (supporting). **Keita Nishitani**: Data curation (equal); Investigation (equal); Methodology (equal); Resources (equal); Writing – review & editing (supporting). **Sergey Pikuz**: Conceptualization (supporting); Data curation (supporting); Formal analysis (supporting); Investigation (equal); Project administration (supporting); Resources (equal); Writing – review & editing (equal). **Masaki Kando**: Conceptualization (equal); Data curation (equal); Formal analysis (supporting); Investigation (equal); Project administration (lead); Software (equal). **Ryosuke Kodama**: Funding acquisition (lead); Investigation (supporting); Supervision (lead). **Kiminori Kondo**: Funding acquisition (lead); Investigation (equal); Project administration (lead); Software (lead). **Mamiko Nishiuchi**: Conceptualization (equal); Data curation (lead); Investigation (equal); Project administration (lead); Writing – review & editing (supporting).

DATA AVAILABILITY

The data presented in this paper are available from the corresponding author on reasonable request.

REFERENCES

[1] M. Baryakhtar, R. Caputo, D. Croon, K. Perez, E. Berti *et al.*, "Dark matter in extreme astrophysical environments," *Proceedings of the U.S. Community Study on the Future of Particle Physics (Snowmass 2021)* (APS Division of Particles and Fields, 2022), CF3, pp. 1–33; arXiv:2203.07984.

04 August 2025 07:51:07

© Author(s) 2024

[2]J. R. Stone, "Nuclear physics and astrophysics constraints on the high density matter equation of state," Universe **7**, 257 (2021).
[3]H. Satz, *Extreme States of Matter in Strong Interaction Physics* (Springer International Publishing, Cham, 2018).
[4]V. E. Fortov, *Extreme States of Matter High Energy Density Physics* (Springer Series in Materials Science, 2016).
[5]E. G. Gamaly, *Femtosecond Laser–Matter Interactions: Solid–Plasma–Solid Transformations at the Extreme Energy Density* (CRC Press, 2022).
[6]D. Levko and L. L. Raja, "High-voltage microdischarge as a source of extreme density plasma," Phys. Plasmas **25**, 013509 (2018).
[7]J. Colvin and J. Larsen, *Extreme Physics: Properties and Behavior of Matter at Extreme Conditions* (Cambridge University Press, 2013).
[8]P.-A. Gourdain, M. Evans, B. Foy, D. Mager, R. McBride *et al.*, "HADES: A high amperage driver for extreme states," arXiv:1705.04411 (2017).
[9]S. H. Glenzer, L. B. Fletcher, E. Galtier, B. Nagler, R. Alonso-Mori *et al.*, "Matter under extreme conditions experiments at the Linac Coherent Light Source," J. Phys. B: At., Mol. Opt. Phys. **49**, 092001 (2016).
[10]G. Mourou, "Nobel Lecture: Extreme light physics and application," Rev. Mod. Phys. **91**, 030501 (2019).
[11]U. Zastrau, K. Appel, C. Baehtz, O. Baehr, L. Batchelor *et al.*, "The high energy density scientific instrument at the European XFEL," J. Synchrotron Radiat. **28**, 1393–1416 (2021).
[12]N. Jourdain, U. Chaulagain, M. Havlík, D. Kramer, D. Kumar *et al.*, "The L4n laser beamline of the P3-installation: Towards high-repetition rate high-energy density physics at ELI-Beamlines," Matter Radiat. Extremes **6**, 015401 (2021).
[13]R. Hollinger, S. Wang, Y. Wang, A. Moreau, M. G. Capeluto *et al.*, "Extreme ionization of heavy atoms in solid-density plasmas by relativistic second-harmonic laser pulses," Nat. Photonics **14**, 607–611 (2020).
[14]H. Kiriyama, Y. Miyasaka, A. Kon, M. Nishiuchi, A. Sagisaka *et al.*, "Laser output performance and temporal quality enhancement at the J-KAREN-P petawatt laser facility," Photonics **10**, 997 (2023).
[15]K. Burdonov, A. Fazzini, V. Lelasseux, J. Albrecht, P. Antici *et al.*, "Characterization and performance of the Apollon short-focal-area facility following its commissioning at 1 PW level," Matter Radiat. Extremes **6**, 064402 (2021).
[16]A. S. Pirozhkov, Y. Fukuda, M. Nishiuchi, H. Kiriyama, A. Sagisaka *et al.*, "Approaching the diffraction-limited, bandwidth-limited Petawatt," Opt. Express **25**, 20486 (2017).
[17]A. A. Soloviev, K. F. Burdonov, V. N. Ginzburg, M. Y. Glyavin, R. S. Zemskov *et al.*, "Research in plasma physics and particle acceleration using the PEARL petawatt laser," Phys.-Usp. **67**, 293–313 (2024).
[18]M. Kalashnikov, A. Andreev, and H. Schönnagel, "Limits of the temporal contrast for CPA lasers with beams of high aperture," Proc. SPIE **7501**, 750104 (2009).
[19]H. Kiriyama, Y. Miyasaka, A. Sagisaka, K. Ogura, M. Nishiuchi *et al.*, "Experimental investigation on the temporal contrast of pre-pulses by post-pulses in a petawatt laser facility," Opt. Lett. **45**, 1100 (2020).
[20]H. Kiriyama, A. S. Pirozhkov, M. Nishiuchi, Y. Fukuda, K. Ogura *et al.*, "High-contrast high-intensity repetitive petawatt laser," Opt. Lett. **43**, 2595 (2018).
[21]A. Faenov, V. Dyakin, A. Magunov, T. Pikuz, I. Skobelev *et al.*, "Using x-ray spectroheliograph technique for investigations of laser-produced plasma under interaction with strong magnetic field," Phys. Scr. **53**, 591–596 (1996).
[22]M. A. Alkhimova, A. Y. Faenov, T. A. Pikuz, I. Y. Skobelev, S. A. Pikuz *et al.*, "X-ray emission from stainless steel foils irradiated by femtosecond petawatt laser pulses," J. Phys.: Conf. Ser. **946**, 012018 (2018).
[23]M. A. Alkhimova, I. Y. Skobelev, A. Y. Faenov, D. A. Arich, T. A. Pikuz *et al.*, "Accounting for the instrument function of crystal spectrometers operating in many reflection orders in the diagnostics of laser plasma from its continuum spectrum," Quantum Electron. **48**, 749–754 (2018).
[24]A. Stafford, A. S. Safronova, A. Y. Faenov, T. A. Pikuz, R. Kodama *et al.*, "Influence of hot electrons on the spectra of iron plasma irradiated by femtosecond laser pulses with 10^{21} W/cm^2 intensities," Laser Part. Beams **35**, 92–99 (2017).
[25]A. Y. Faenov, I. Y. Skobelev, T. A. Pikuz, S. A. Pikuz, R. Kodama *et al.*, "Diagnostics of warm dense matter by high-resolution X-ray spectroscopy of hollow ions," Laser Part. Beams **33**, 27–39 (2015).
[26]O. Renner, I. Uschmann, and E. Förster, "Diagnostic potential of advanced X-ray spectroscopy for investigation of hot dense plasmas," Laser Part. Beams **22**, 25–28 (2004).
[27]A. Y. Faenov, T. A. Pikuz, I. Y. Skobelev, A. I. Magunov, V. P. Efremov *et al.*, "X-ray spectroscopic observations of a superdense plasma in nanoparticles irradiated by superintense femtosecond laser radiation," J. Exp. Theor. Phys. **80**, 730–733 (2004).
[28]J. Colgan, A. Y. Faenov, S. A. Pikuz, E. Tubman, N. M. H. Butler *et al.*, "Evidence of high-n hollow-ion emission from Si ions pumped by ultraintense x-rays from relativistic laser plasma," Europhys. Lett. **114**, 35001 (2016).
[29]S. N. Ryazantsev, I. Y. Skobelev, A. S. Martynenko, M. A. Alkhimova, M. D. Mishchenko *et al.*, "Analysis of Ly$_\alpha$ dielectronic satellites to characterize temporal profile of intense femtosecond laser pulses," Crystals **11**, 130 (2021).
[30]A. Y. Faenov, J. Colgan, S. B. Hansen, A. Zhidkov, T. A. Pikuz *et al.*, "Nonlinear increase of X-ray intensities from thin foils irradiated with a 200 TW femtosecond laser," Sci. Rep. **5**, 13436 (2015).
[31]E. Oks, E. Dalimier, A. Y. Faenov, P. Angelo, S. A. Pikuz *et al.*, "Using X-ray spectroscopy of relativistic laser plasma interaction to reveal parametric decay instabilities: A modeling tool for astrophysics," Opt. Express **25**, 1958 (2017).
[32]T. Nagayama, J. E. Bailey, G. P. Loisel, G. A. Rochau, J. J. MacFarlane *et al.*, "Numerical investigations of potential systematic uncertainties in iron opacity measurements at solar interior temperatures," Phys. Rev. E **95**, 063206 (2017).
[33]See https://Prism-Cs.Com/Software/PrismSPECT/Overview.Html for more information about PrismSPECT.
[34]J. J. MacFarlane, I. E. Golovkin, P. R. Woodruff, S. K. Kulkarni, and I. M. Hall, "Simulation of plasma ionization and spectral properties with PrismSPECT," in *2013 Abstr. IEEE Int. Conf. Plasma Sci.* (IEEE, 2013), p. 1.
[35]M. A. Alkhimova, A. Y. Faenov, I. Y. Skobelev, T. A. Pikuz, M. Nishiuchi *et al.*, "High resolution X-ray spectra of stainless steel foils irradiated by femtosecond laser pulses with ultra-relativistic intensities," Opt. Express **25**, 29501 (2017).
[36]P. W. Hatfield, J. A. Gaffney, G. J. Anderson, S. Ali, L. Antonelli *et al.*, "The data-driven future of high-energy-density physics," Nature **593**, 351–361 (2021).

04 August 2025 07:51:07

© Author(s) 2024